

Supporting Information for “Investigation of Metal Oxide Anode Degradation in Lithium-ion Batteries via Identical-Location TEM”

Neil Spinner[†], Lichun Zhang[‡], and William E. Mustain^{†,*}

[†]Department of Chemical & Biomolecular Engineering, University of Connecticut, Storrs, CT, 06269, United States

[‡]Institute of Materials Science, University of Connecticut, Storrs, CT, 06269, United States

*Corresponding author email: mustain@enr.uconn.edu

1. Anodes Labeled by Reaction Mechanism

 = Conversion
 = Intercalation
 = Alloying

										5 B	6 C	7 N
										13 Al	14 Si	15 P
3 Li	22 Ti	23 V	24 Cr	25 Mn	26 Fe	27 Co	28 Ni	29 Cu	30 Zn	31 Ga	32 Ge	33 As
	40 Zr	41 Nb	42 Mo	43 Tc	44 Ru	45 Rh	46 Pd	47 Ag	48 Cd	49 In	50 Sn	51 Sb

Figure S1. Candidate elements whose pure species and oxides function as lithium-ion battery anodes labeled according to anode reaction mechanism: conversion, intercalation, or alloying.

2. Experimental Details

2.1. OMNiO Synthesis

Ordered mesoporous nickel oxide (OMNiO) was fabricated using a template-based synthesis technique which is illustrated in Figure S2. First, a mesoporous silica template (SBA-15) was synthesized using a previously-published technique [1,2]. Briefly, Pluronic P123 (BASF) triblock copolymer was dissolved in a solution of HCl and deionized water (Millipore Direct-Q 3UV, 18.2 MΩ). After addition of tetraethyl orthosilicate and two separate heating stages (20h at 45°C and 24h at 100°C), the template was washed and filtered with ethanol and deionized water, followed by drying under vacuum and calcination in air at 500°C for 3h.

OMNiO was prepared using a wet impregnation method with the SBA-15 template. Aqueous 0.5M Ni(NO₃)₂ (Acros, 99%) was added dropwise to dry SBA-15 until a ratio of approximately 6.3 mL of 0.5M Ni(NO₃)₂ per g SBA-15 was achieved. The resulting gel was stirred manually until homogeneous, followed by calcination in air at 400°C for 3.5h. Template

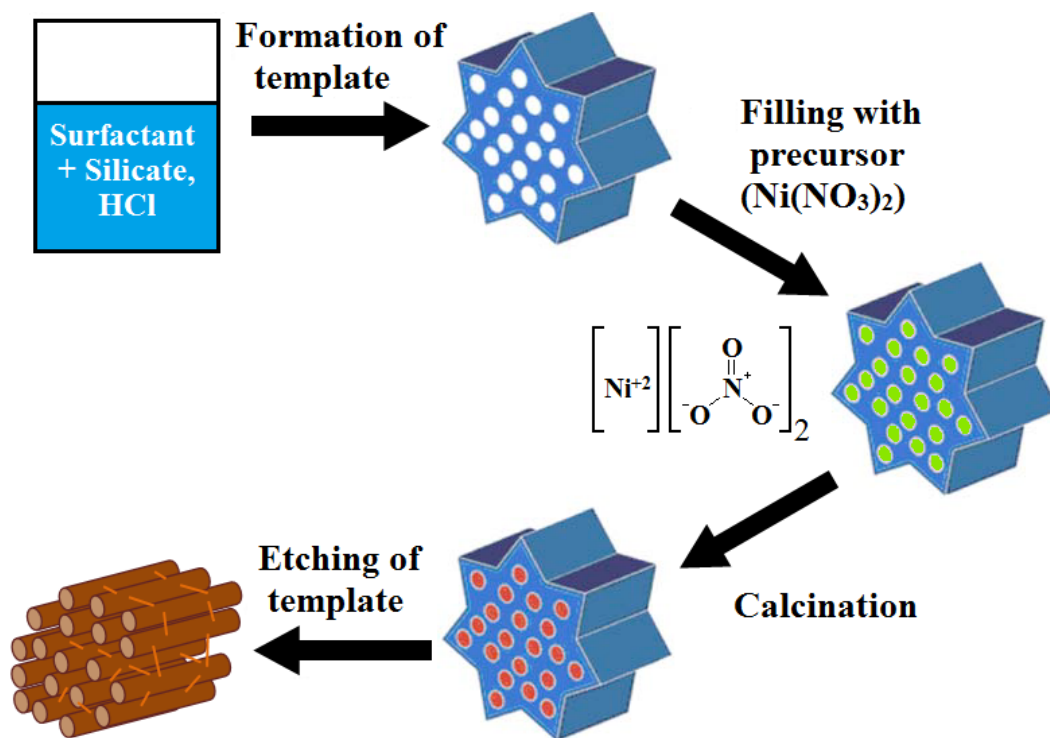


Figure S2. Schematic for synthesis of ordered mesoporous nickel oxide (OMNiO). Adapted from [1].

was then removed using two identical etching steps in hot (100°C) 5M KOH for 24h each, along with a thorough deionized water rinse in between. The OMNiO was then rinsed once more with copious deionized water and dried.

2.2. Anode Fabrication

Anodes were fabricated by preparing inks with varying amounts of OMNiO, carbon black (Vulcan XC-72R, Cabot), and polyvinylidene fluoride (PVDF) binder (Kynar blend) dispersed in N-methylpyrrolidone (NMP) solvent (Acros, 99.5% Extra Dry) through successive sonication and stirring steps until homogeneous. A copper foil (Alfa Aesar, 99.999%) was used as the current collector, and prior to ink deposition it was mechanically roughened and rinsed with isopropanol (Fisher, Optima). The ink was then sprayed onto the Cu foil to a uniform thickness, followed by heating under vacuum at 100°C for 24h. The electrode was then pressed at 1500 lbs and massed. Active loadings of anodes were around 0.5-2.0 mg/cm².

2.3. Coin Cell Fabrication

Batteries were tested using 2.0 cm diameter coin cells (Hohsen Corp.) with lithium metal (Alfa Aesar, 99.9%) as the cathode and Celgard 2320 trilayer PP/PE/PP as the separator. The electrolyte used for all tests was 1M lithium hexafluorophosphate (LiPF₆, Acros 98%) in a solution of (1:1:1) volume ratio ethylene carbonate (EC, Acros 99+%):dimethyl carbonate (DMC, Acros 98+%):diethyl carbonate (DEC, Acros 99%). 15 μL of electrolyte was applied to each side of the separator, which was punched to a 1.9 cm diameter circle, while the anode and

cathode were punched to 1.5 cm diameter coins. All coin cells were constructed inside an argon-purged glove box (Labconco).

2.4. Physical and Electrochemical Characterization

Coin cells were cycled using charge-discharge tests at a rate of C/5 (based on theoretical capacity of 718 mAh/g for NiO) between 0.001 – 3.0V vs. Li/Li⁺ using an Arbin MSTAT battery test system. All other electrochemical tests were performed using an Autolab PGSTAT302N Potentiostat (Eco Chemie). Electrochemical Impedance Spectroscopy (EIS) was conducted between 100kHz – 50mHz with a 5mV amplitude at the coin cell open circuit voltage. Cyclic Voltammetry (CV) was performed between 0.001 – 3.0V at a scan rate of 0.1mV/s. Transmission Electron Microscopy (TEM) was conducted using a JEOL 2010 FasTEM. X-ray Diffraction (XRD) was performed using a Bruker D8 Advance X-ray Diffractometer with Cu K α_1 radiation ($\lambda = 0.154$ nm). Brunauer-Emmett-Teller (BET) specific surface area analysis and N₂ adsorption isotherms were obtained using a Micromeritics ASAP 2020 system. Samples were degassed under vacuum at 150°C for 16h prior to N₂ adsorption.

2.5. Identical-Location TEM Grid Experiments

For identical-location TEM experiments, a 3mm diameter copper TEM finder grid (Ted Pella, Inc., 100 mesh) was lightly sprayed with an OMNiO ink containing 10% PVDF binder and dried on a hot plate at 100°C. After initial TEM imaging, the Cu grid was cycled using a

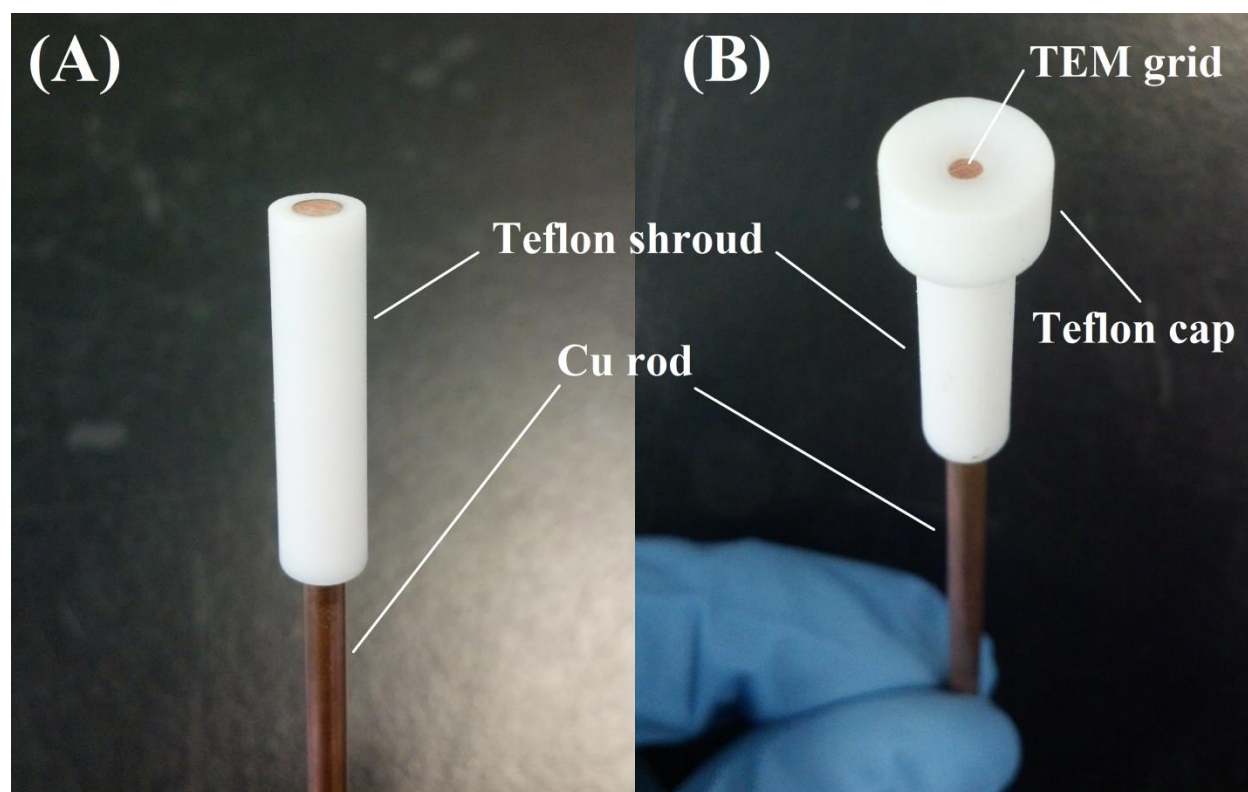


Figure S3. Pictures of (A) Teflon-shrouded copper rod electrode alone and (B) electrode with Teflon cap holding Cu TEM grid in place.

custom-built Teflon-shrouded copper electrode with a Teflon cap, which is pictured in Figure S3 (schematic is also depicted in Figure 3A-B in main document). The cap applied pressure to the grid to ensure contact with the Cu electrode and overall electronic conductivity, and also facilitated electrolyte access to the TEM grid via the tapered opening in the center. Inside the argon-purged glove box, the electrode/TEM grid setup was pressed into a strip of Celgard and lithium metal and dipped into a beaker containing (1:1:1)EC:DMC:DEC electrolyte. Two CVs were then performed between 0.001 – 3.0V at 0.1mV/s to cycle the OMNiO particles, and then the electrode/TEM grid setup was gently dried without rinsing to prevent excessive particle detachment. After a second stage of TEM imaging, five more CVs were performed followed by a final set of TEM images.

A considerable IR resistance was observed for CVs obtained using the electrode/TEM grid configuration, which was expected, and as a result CVs have not been included in this work. It is well known that pressure on the anode and cathode into the separator is pivotal to lithium-ion battery performance. However, this pressure was simply not possible with the electrode/TEM grid setup due to potential particle detachment resulting from physical contact with the separator. For this reason, a small gap was maintained between the anode (NiO-coated TEM grid) and separator via the concavity of the Teflon cap (shown in Fig. S3). This small volume of electrolyte contributed to the sizeable IR resistance in the CVs.

3. Physical Characterization

3.1. XRD, BET, N₂ Adsorption Isotherm and Pore Size Distribution

Figure S4 shows the XRD spectrum for OMNiO. Peak positions for NiO, along with corresponding crystal faces, were identified at 37.2° (111), 43.2° (200), 62.8° (220), 75.3° (311), and 79.3° (222) [3,4]. The Scherrer Equation was used to estimate the OMNiO average grain boundary size, Equation S1:

$$D = \frac{k\lambda}{\beta \cos \theta} \quad (\text{S1})$$

where D is the grain boundary size, k is the shape factor (taken as 0.89), λ is the X-ray wavelength, β is the peak width at half the maximum, and θ is the Bragg angle. Applying Eq. S1 to the first three peaks, the average grain boundary size was 18.5nm.

N₂ adsorption isotherm and pore size distribution data for OMNiO are shown in Figure S5. The BET specific surface area (obtained from the monolayer adsorption region between values of P/P_0 of 0.05 to 0.2) was 80.4 m²/g, and along with the Scherrer Equation average grain boundary size, these values were comparable to those found in the literature for similar template-based NiO nanoparticles [5-7]. The isotherm seen in Fig. S5A exhibited type IV behavior with a hysteresis loop at higher relative pressures, which resulted from capillary condensation in mesopores [1,8]. The extension of the hysteresis loop to relative pressures of around 0.7 – 0.75 indicated a varying range of mesopore sizes, which was also confirmed by the pore size distribution seen in Fig. S5B [1,8]. A bimodal distribution was observed with a sharp peak around 3.3nm and a broad peak around 25-35nm. This likely occurred due to partial expulsion of Ni(NO₃)₂ from the SBA-15 template via melting/redistribution during calcination, resulting in larger, agglomerated NiO particles that crystallized outside the template walls [9]. This may also

explain the small discrepancy between apparent nanoparticle sizes observed in TEM images (ca. 8-10nm) and the larger average grain boundary size calculated from the Scherrer Equation (18.5nm).

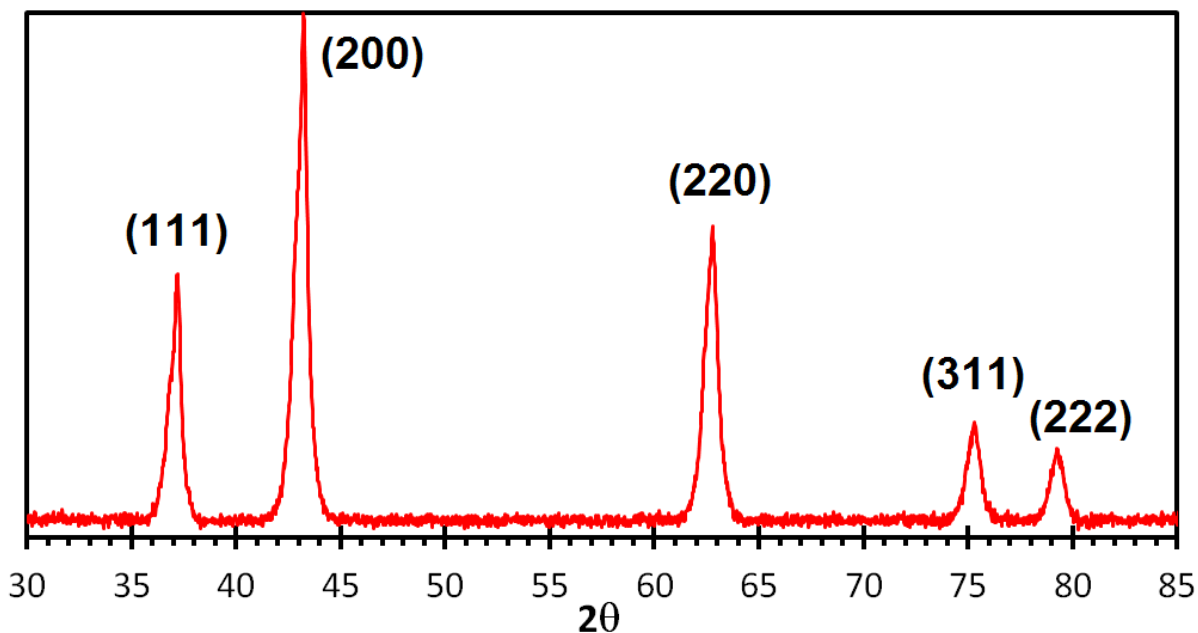


Figure S4. XRD spectrum for OMNiO. Acquisition rate was $1.3^\circ/\text{min}$.

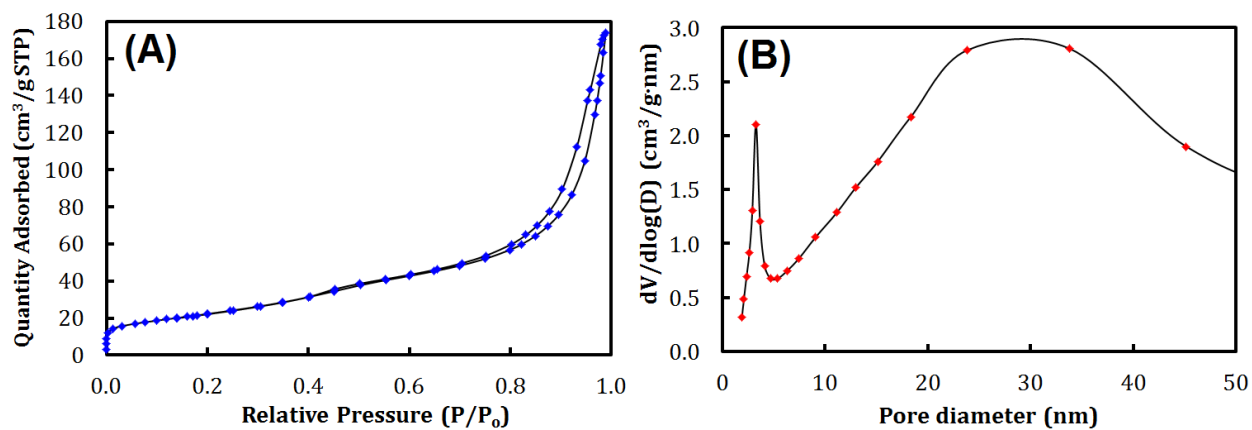


Figure S5. (A) N_2 adsorption isotherm and (B) pore size distribution for OMNiO.

4. Results and Discussion

4.1. Additional TEM Images

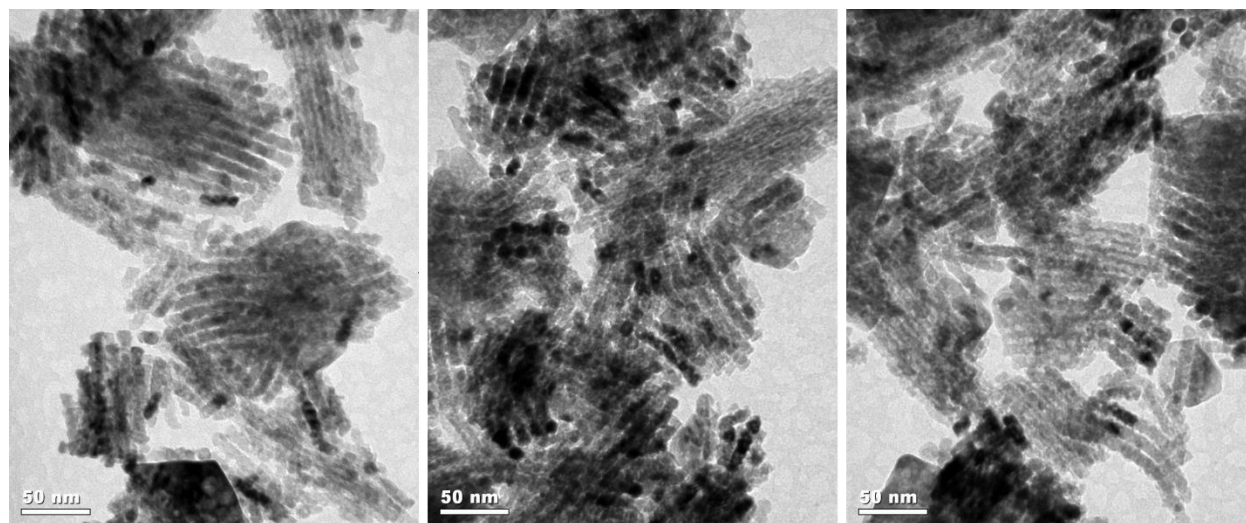


Figure S6. Additional TEM images of OMNiO.

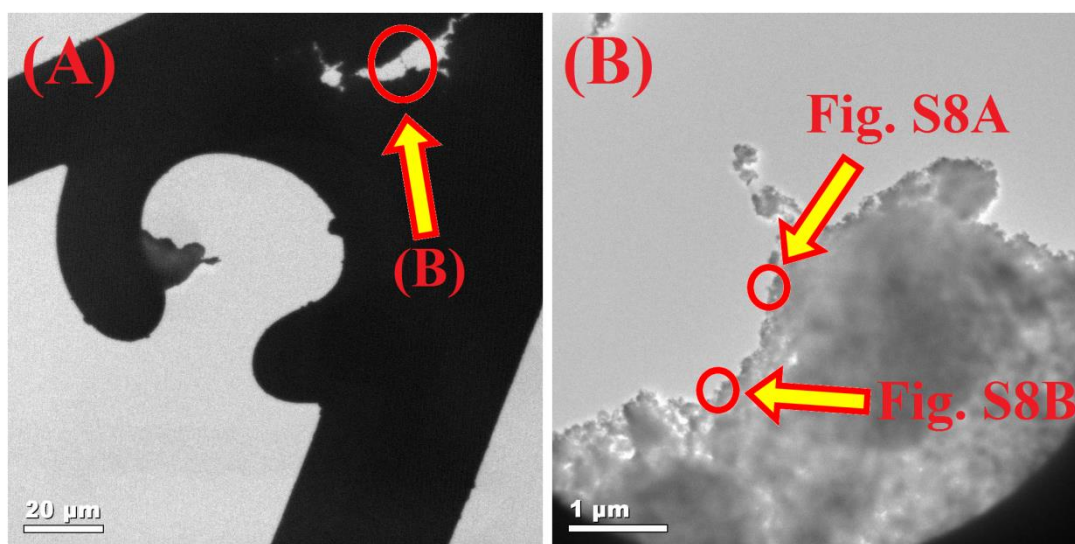


Figure S7. Progression of spots for identical-location TEM images for OMNiO.

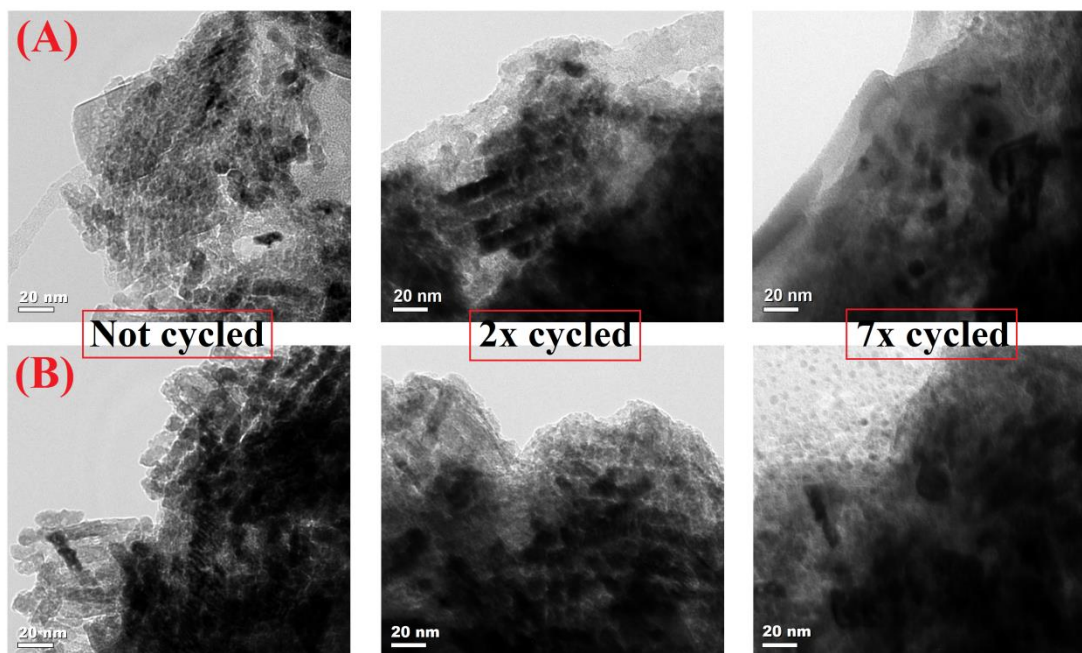


Figure S8. Identical-location TEM images for OMNiO on a Cu TEM grid. Images obtained before cycling, after two cycles, and after seven total cycles at 0.1mV/s between 0.001-3.0V.

4.2. Carbon Black Charge-Discharge

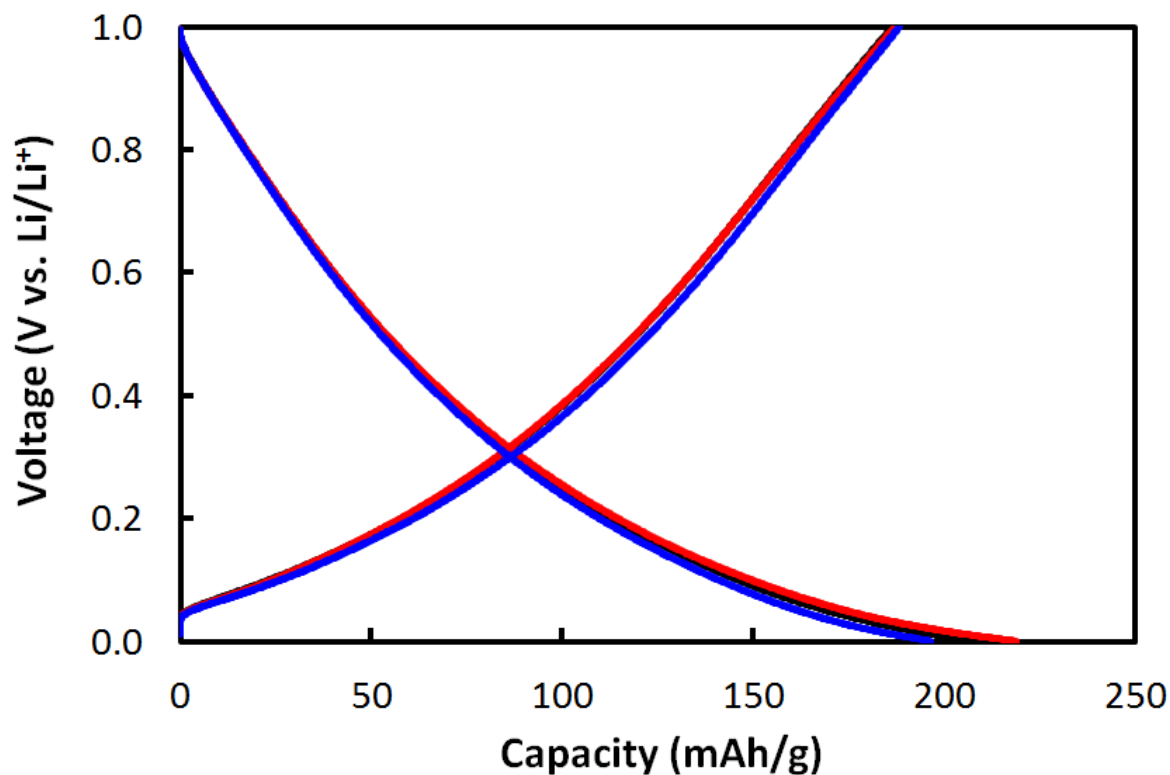


Figure S9. Charge-discharge curves for plain carbon black anode with 10% binder at C/5 rate.

Figure S9 shows charge-discharge curves for the carbon black conductive additive as an anode by itself (with 10% PVDF binder). No voltage plateau was observed, which was expected, and this suggested a lack of Li^+ intercalation into the carbon structure. However, sloping curves repeatedly reaching about 200 mAh/g likely resulted from electrolyte decomposition and a more stable SEI formation over the high surface area carbon, creating secondary Li^+ storage sites and accounting for the boost in OMNiO capacity above the theoretical value observed in anodes containing 40% carbon (Fig. 2C-D in main document) [10,11].

4.3. OMNiO with 40% Carbon Identical-Location TEM

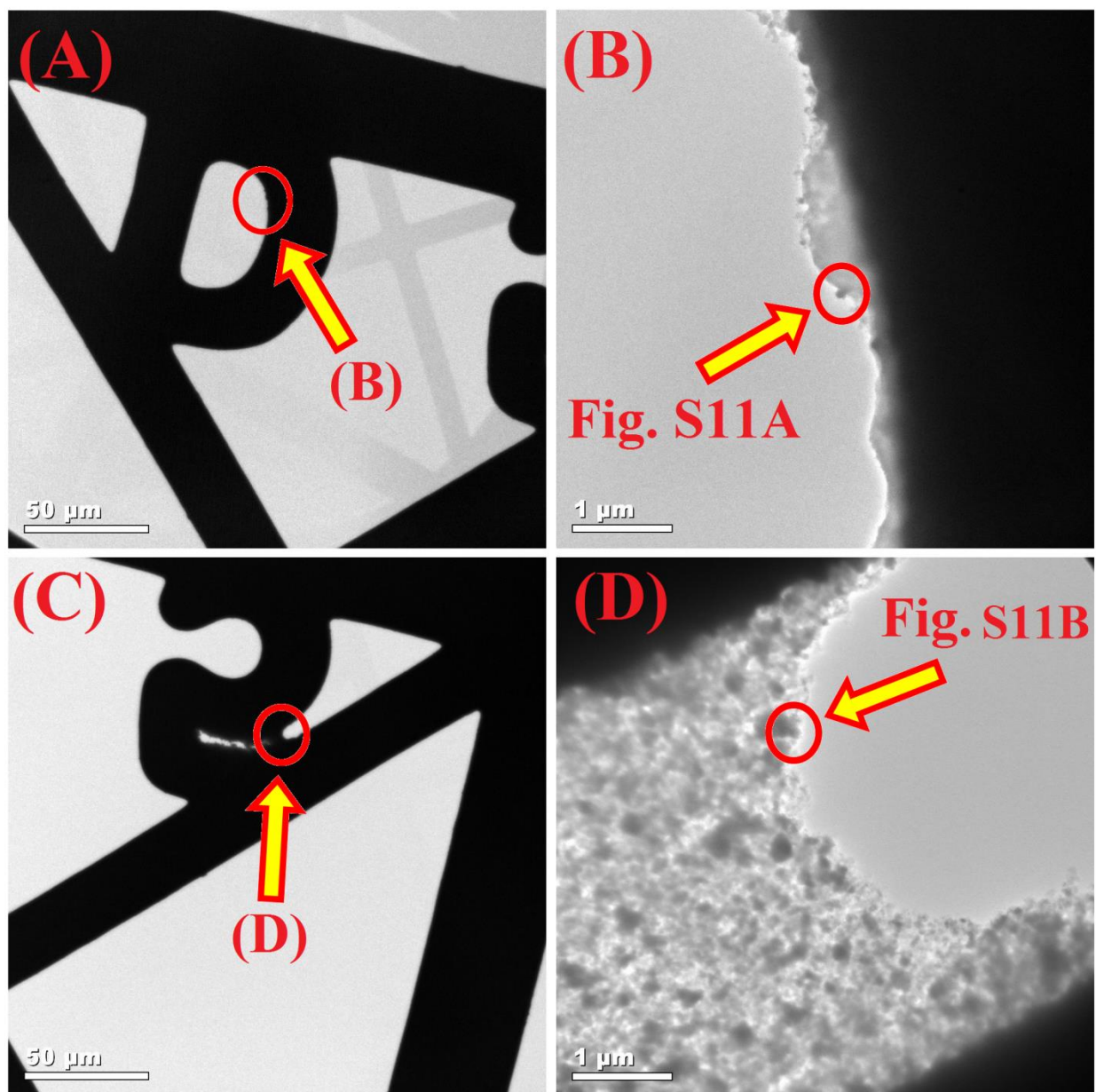


Figure S10. Progression of spots for identical-location TEM images for OMNiO with 40% carbon black.

Figure S10 shows the progression of spots used for identical-location TEM images for OMNiO with 40% carbon black, and the corresponding TEM images before and after two cycles are shown in Figure S11. Surprisingly, after only two cycles the ordered mesoporous structure was completely absent, compared to the plain OMNiO which largely retained its structure through two cycles, only showing dramatic structural degradation after seven cycles. This result was in stark contrast to the superior capacity retention observed in Fig. 2D (main document), and suggests that structure alone may not be the only contributor to performance losses. The presence of 40% carbon black likely improved overall conductivity enough to ensure cyclability even after almost complete degradation of the original OMNiO mesoporous structure.

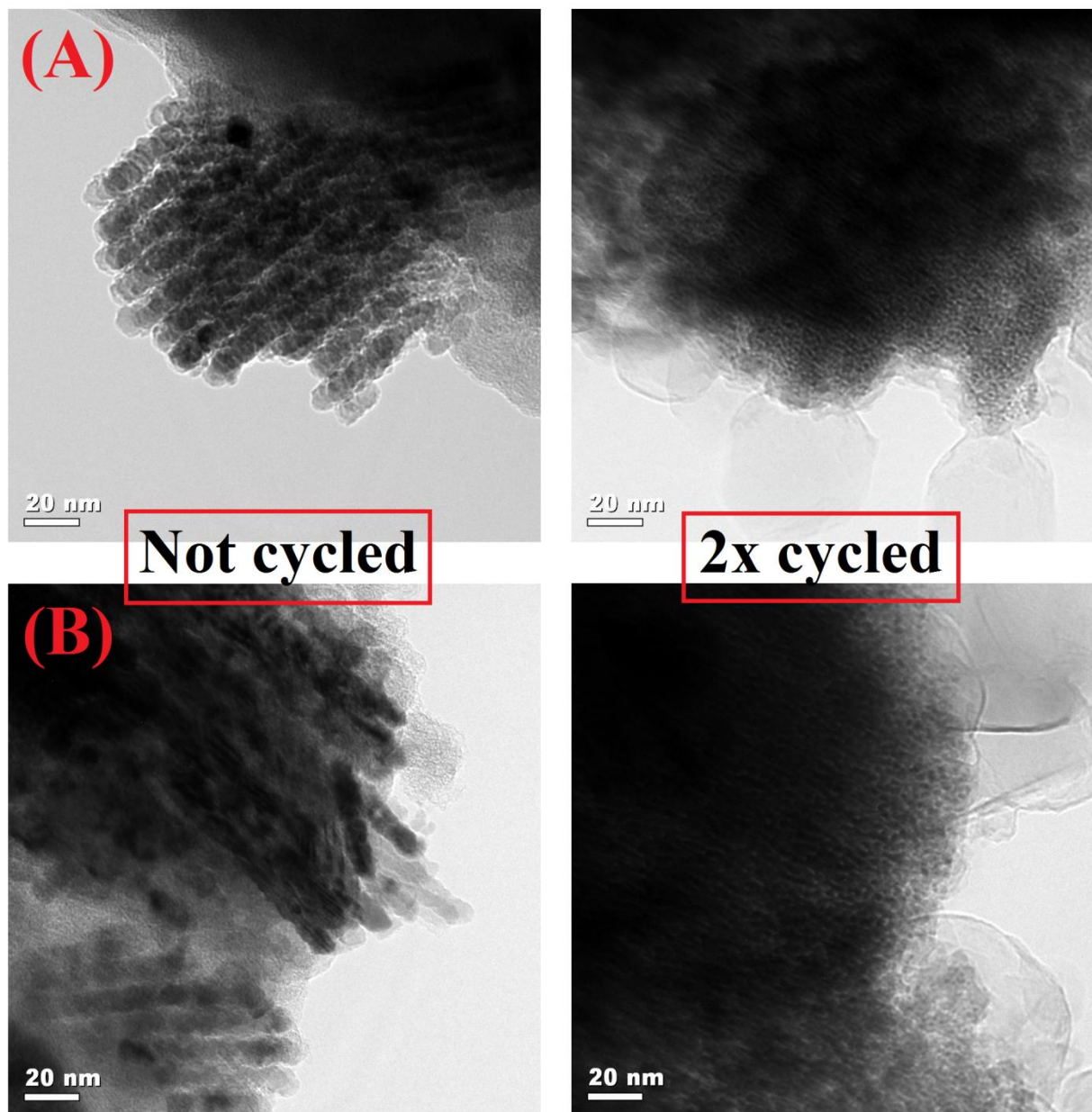


Figure S11. Identical-location TEM images for OMNiO with 40% carbon black on a Cu TEM grid. Images obtained before cycling and after two cycles at 0.1mV/s between 0.001-3.0V.

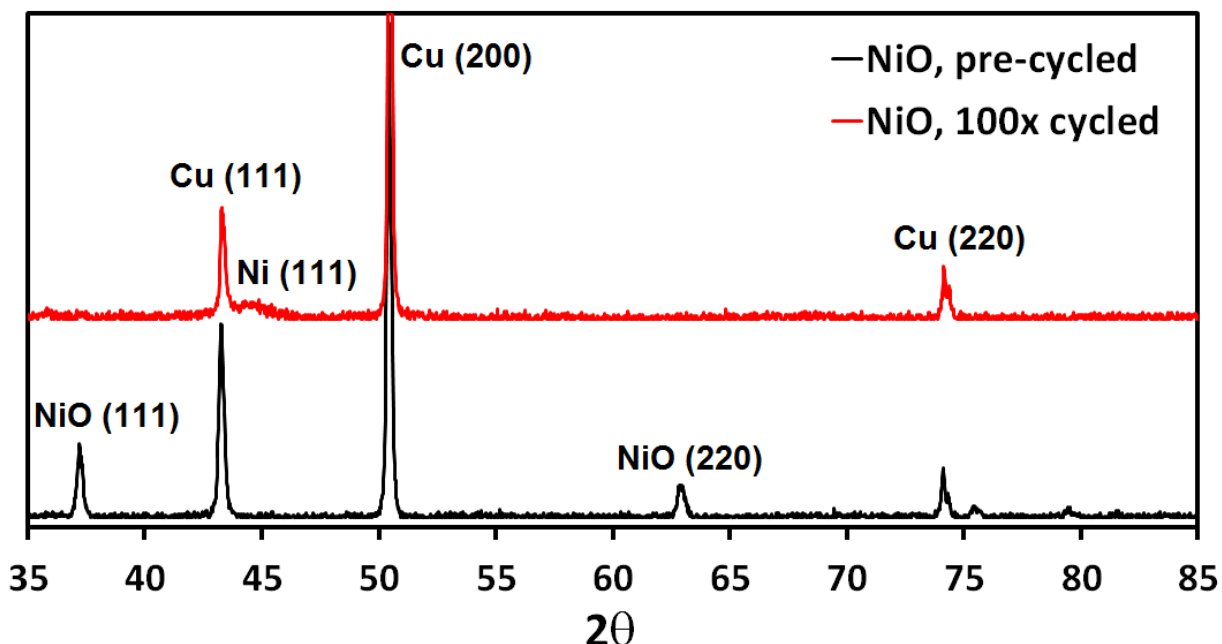


Figure S12. XRD spectra for NiO on Cu foil anode before and after 100 charge-discharge tests at C/5 rate. Acquisition rate was 1.3°/min.

To further illustrate the connection between structure and conductivity, XRD was performed on a NiO electrode before and after 100 charge-discharge cycles, and Figure S12 shows the resulting spectra (details for synthesis of NiO can be found in references [3] and [12]). Before cycling, clear peaks for NiO were identified at 37.2° (111), 42.9° (200), and 62.9° (220) [3], and for the Cu current collector at 42.9° (111), 50.4° (200) and 74.1° (220) [13]. However, after cycling, the peaks for NiO were absent, and instead a low, broad peak around 44.5° was visible and corresponded to the (111) crystal face for metallic Ni [14]. This showed that the NiO became essentially “stuck” in the charged state, likely resulting from large, inactive Li₂O growth from the NiO conversion reaction [15]. Electronically-inactive Li₂O formed from NiO conversion, thus connecting structural degradation to capacity loss; however, the root cause can be tied to the lack of conductivity of Li₂O, which was corroborated by the retention in capacity shown in this work despite broad structural degradation.

4.4. EIS

EIS was performed on OMNiO coin cells with varying amounts of carbon black added, and the corresponding Nyquist plots are shown in Figure S13. Several conclusions can be drawn from the data shown in Fig. S13: the leftmost, high frequency Z_r (x-axis) intercept corresponded to the Ohmic resistance of the electrolyte; the semicircle(s) at medium frequencies corresponded to the charge transfer resistances of the SEI film and/or Li⁺ transport at the electrode/electrolyte interface; and the inclined line at low frequency corresponded to the Warburg impedance of Li⁺ ion diffusion in the electrode [16,17]. For all anodes, the electrolyte resistance observed was virtually negligible. Two distinct semicircles could be fitted to all anodes, and the widths of these can be attributed to the SEI and Li⁺ charge-transfer resistances, respectively [16,17]. The

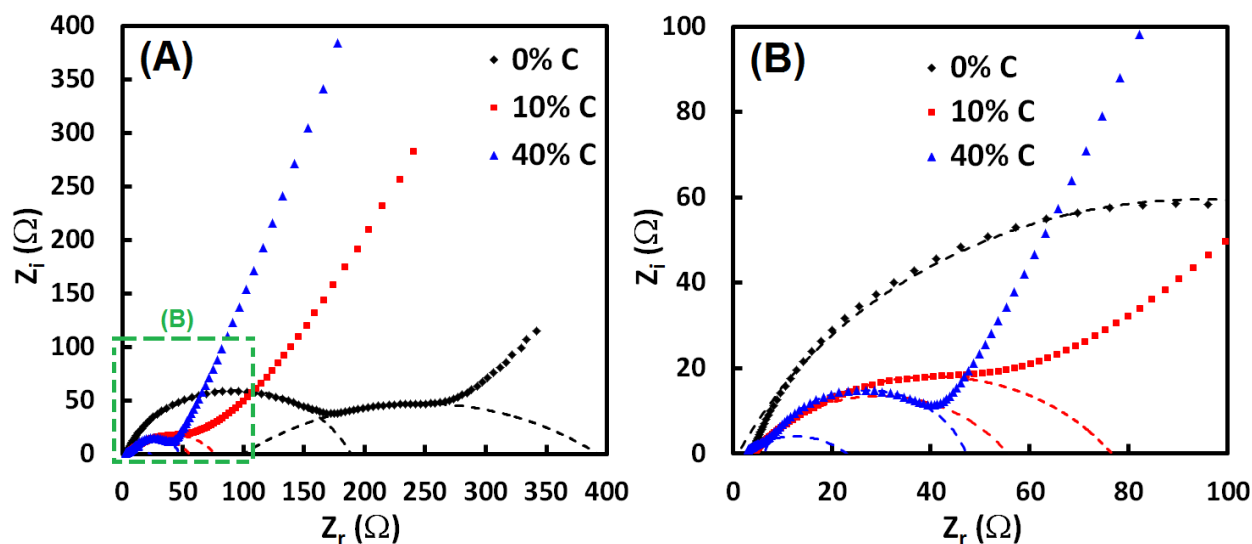


Figure S13. EIS Nyquist plots for OMNiO anode coin cells with 0%, 10% and 40% carbon black. (B) shows green boxed section zoomed in. Batteries were cycled three times each at a 1C charge-discharge rate, and then allowed to rest several hours until a stable voltage was reached before conducting impedance tests. EIS was taken at the battery's open circuit voltage between frequencies of 100kHz – 50mHz with a 5mV voltage amplitude.

widths of the first semicircle for 0%, 10% and 40% were found to be 188 Ω , 52 Ω and 21 Ω , respectively, and the widths of the second semicircle for 0%, 10% and 40% were found to be 293 Ω , 72 Ω and 41 Ω , respectively. This clear trend of decreasing charge transfer resistances for both the SEI and Li⁺ transport as the carbon black percentage increased corresponded to the increase overall conductivity in the anode.

The second distinct trend observed in Fig. S13 was in the low frequency Warburg impedance region. The angle of the inclined line was approximately 45° for the 0% carbon anode, however the slope increased to around 61° for the 10% carbon anode and to 71° for the 40% carbon anode. The increase in angle of the Warburg impedance region can be attributed to a diffusion process in a porous layer that is approaching pure capacitive behavior (which is represented by a vertical line) [18,19]. This may suggest that in addition to better conductivity and reduced charge transfer resistance, increasing the carbon percentage in the anode also improved the Li⁺ diffusion via the pore structure of the carbon black additive [20].

It is clear that conductivity plays a key role in the cyclability and performance of the OMNiO anodes studied in this work. The losses in capacity, which were tied to structural degradation via identical-location TEM and XRD results, seem to be in fact more strongly connected to anode conductivity than simply structural degradation. This was evidenced by greater capacity retention, higher overall capacities, decreased charge transfer resistances, and improved porous layer Li⁺ diffusion observed with an increased carbon black percentage, despite the accelerated structural degradation seen with 40% carbon black. Therefore, in future research of metal oxide anodes, an increased focus on improving and maintaining electrode conductivity, in addition to particle structure, during extended charge-discharge cycles could lead to great strides in lithium-ion battery technology.

5. References

- [1] S. Shrestha and W. E. Mustain, *J. Electrochem. Soc.*, 2010, **157**, B1665.
- [2] S. Shrestha, S. Asheghi, J. Timbro and W. E. Mustain, *Carbon*, 2013, **60**, 28.
- [3] N. Spinner and W. E. Mustain, *Electrochim. Acta*, 2011, **56**, 5656.
- [4] N. Spinner and W. E. Mustain, *J. Electrochem. Soc.*, 2012, **159**, E187.
- [5] F. Jiao, A. H. Hill, A. Harrison, A. Berko, A. V. Chadwick and P. G. Bruce, *J. Am. Chem. Soc.*, 2008, **130**, 5262.
- [6] H. Liu, G. Wang, J. Liu, S. Qiao and H. Ahn, *J. Mater. Chem.*, 2011, **21**, 3046.
- [7] H.-Q. Lu, L. Shi, W.-Z. Weng, C.-J. Huang and H.-L. Wan, *Acta Phys. -Chim. Sin.*, 2012, **28**, 2697.
- [8] K. S. W. Sing, *Pure & Appl. Chem.*, 1982, **54**, 2201.
- [9] E. Marceau, M. Che, J. Čejka and A. Zukal, *ChemCatChem*, 2010, **2**, 413.
- [10] M. B. Pinson and M. Z. Bazant, *J. Electrochem. Soc.*, 2013, **160**, A243.
- [11] J. H. Pan, Q. Huang, Z. Y. Koh, D. Neo, X. Z. Wang and Q. Wang, *ACS Appl. Mater. Interfaces*, 2013, **5**, 6292.
- [12] N. Spinner and W. E. Mustain, *J. Electroanal. Chem.*, 2013, **711**, 8.
- [13] J. Zhong, W. Xiang, H. Zhao, W. Zhao, G. Chen and X. Liang, *J. Alloys Compd.*, 2012, **537**, 269.
- [14] N. Mahata, A. F. Cunha, J. J. M. Órfão and J. L. Figueiredo, *Chem. Eng. J.*, 2012, **188**, 155.
- [15] P. Poizot, S. Laruelle, S. Grugeon, L. Dupont and J.-M. Tarascon, *Nature*, 2000, **407**, 496.
- [16] A. K. Rai, L. T. Ahn, C.-J. Park and J. Kim, *Ceram. Int.*, 2013, **39**, 6611.
- [17] S. Yang, H. Song and X. Chen, *Electrochem. Commun.*, 2006, **8**, 137.
- [18] O. Devos, C. Gabrielli and B. Tribollet, *Electrochim. Acta*, 2006, **51**, 1413.
- [19] Y. Yamada, T. Sasaki, N. Tatsuda, D. Weingarth, K. Yano and R. Kötz, *Electrochim. Acta*, 2012, **81**, 138.
- [20] B. Liu and S. Creager, *J. Power Sources*, 2010, **195**, 1812.